35th Annual International Conference of the IEEE EMBS
Osaka, Japan, 3 - 7 July, 2013

# Model-based segmentation of the middle phalanx in digital radiographic images of the hand

Ronald Dendere, Gordian Kabelitz, and Tania S. Douglas, *Senior Member, IEEE*

***Abstract*—We present techniques for segmenting the middle phalanx of the middle finger in digital radiographic images using deformable models and active shape models (ASMs). The result of segmentation may be used in the estimation of bone mineral density which in turn may be used in the diagnosis of osteoporosis. A technique for minimizing user dependence is described. The segmentation accuracy of the two methods is assessed by comparing contours produced by the algorithms to those produced by manual segmentation, using the Hausdorff distance measure. The ASM technique produces more accurate segmentation.**

## I. Introduction

Osteoporosis is a skeletal disease characterized by low bone mass and micro-architectural deterioration of bone tissue, with a consequent increase in bone fragility and susceptibility to fracture [1]. It is diagnosed by measuring bone mineral density (BMD) and comparing it with the mean of a sex-matched, young and healthy group. Dual energy X-ray absorptiometry (DEXA) is the most common technique, and is considered the gold standard, for the measurement of BMD due to its low radiation dose and proven ability to predict fracture risk [2-4]. The World Health Organisation (WHO) definition of osteoporosis is based on spine, hip or forearm DEXA measurements of BMD and suggests that BMD measurements should be taken at these skeletal sites since they are the most common sites for osteoporotic fractures. However, osteoporosis affects the entire skeleton [5] and any skeletal site can be used to evaluate the initial fracture risk for the common fracture sites [6-7]. The hand, unlike the spine and hip, is far from organs with higher susceptibility to the effects of ionizing radiation and therefore BMD measurement taken in the hand would result in reduced effective dose. The phalanges are a particularly useful site because bone there is surrounded by little soft tissue, which may result in less accurate BMD measurements. Assessment of phalangeal BMD by DEXA or radiographic absorptiometry (RA) may have long-term value in predicting the risk of both hip and spine fracture [7]. DEXA has been shown to be a useful and accurate method for measuring BMD in hand bones [8-10] and phalangeal DEXA is potentially useful for clinical diagnosis of osteoporosis [9].

Precise segmentation of the region of interest (ROI) is crucial for correct and accurate BMD measurements using DEXA [11]. Region- [12], classification- [13-14] and threshold-based [15] segmentation techniques have been used to segment various bones in radiographic images. We apply active shape models (ASM) [16] and deformable models [17] for segmentation of the middle phalanx of the middle finger in digital radiographic images of the left hand. Both methods have been employed successfully in the segmentation of the middle phalanx of the middle finger in hand images [9; 18]. We introduce a technique that fully automates the segmentation for a deformable model and requires minimal user interaction for an ASM. We use the Hausdorff distance to assess the accuracy of the two methods compared with manual segmentation.

## II. Methods

### A. Materials and X-ray scanning

All images were taken using the Lodox Statscan digital radiographic machine (Lodox Systems, South Africa). The tube settings used for all scans was 100kVp and 50mA. The scan area was from just below the proximal interphalangeal joint to the tip of the middle finger. Images were captured and saved in DICOM format with 14bit depth and a 2100×1990 pixel size.

### B. Preprocessing and automatic location of ROI

The first stage in the processing of the images was to enhance the contrast using a histogram equalisation technique. The second stage involved automatically locating the middle finger in the image and approximation of the centroid of the middle phalanx. The image was thresholded using Otsu's method [19] and at this point, all fingers are detected. In a normal subject, the middle finger would be the largest and therefore the largest detected object is assumed to be the middle finger. The finger is then automatically re-oriented in the image so that it is approximately parallel to edge of the image. Pixel values in each column are summed and the column with the highest sum gives the approximate position of the midline through the middle finger since this is expected to have the highest number of bone pixels as shown in Fig. 1. Assuming that the middle finger covers more than half the length of the image, we use a pixel that is located at the halfway mark of the column with the highest sum as the seed point for a region growing algorithm to identify all bone pixels. Summing row pixel values in the new image with non-zero values for bone pixels yields a profile with two

Research supported by Lodox Systems (South Africa) and the Technology and Human Resources for Industry Programme (THRIP) of the National Research Foundation in South Africa.

Ronald Dendere is a PhD student in the Biomedical Engineering programme at the University of Cape Town, South Africa.

Gordian Kabelitz is an MSc student in Medical Engineering, Section Computer Sciences, University of Lübeck, Germany

Tania S. Douglas is with the Biomedical Engineering Programme and the MRC/UCT Medical Imaging Research Unit, University of Cape Town, Observatory 7925, South Africa. (tania@ieee.org).

distinct sharp transitions as shown in Fig. 2. A search for the sharp changes of grey level starting from the seed point in both directions in the *x*-direction is conducted in order to find the approximate borders of the bone in this row. The mid-point between the bone borders at this level is *x*-coordinate of the middle point of the bone. The length of the middle phalanx at this *x*-position is found from the image containing bone pixels only; the halfway point is the *y*-coordinate of the middle point of the bone.

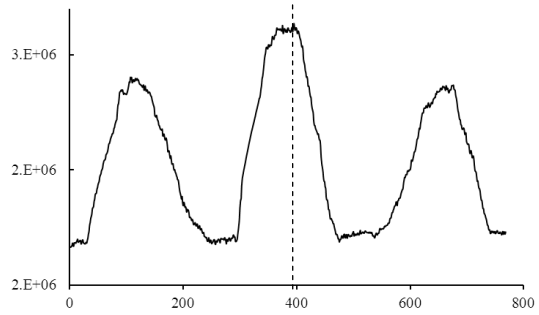


**Figure 1. Summation of image columns (y-axis) against column number (x-axis) - dashed line represents the position of the peak**

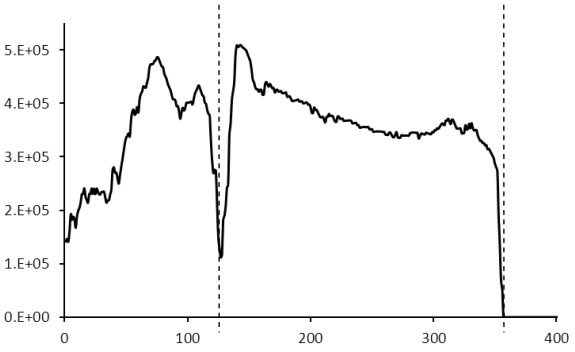


**Figure 2. Summation of image rows (y-axis) against row number (x-axis) - the dashed lines represent the position of the borders of the bone**

### *C. Deformable Model-based Segmentation*

A parametric deformable model was chosen over a geometric one due to the computational complexity of the latter. A Lagrangian formulation is used for explicitly representing parametric models as parameterized curves while Eulerian formulation is used for implicitly representing geometric deformable models using level sets of 2-D distance functions. A parametric deformable model can be mathematically defined as follows:

$$V(s) = (x(s), y(s)) \quad s \in [0,1] \quad (1)$$

where s can be any parameter, the most commonly used parameter is arc length. The model is represented by two vectors that contain the spatial coordinates of points on the contour. A parametric model minimises the weighted sum of internal energy of the model and external energy computed from image data. This yields internal and external forces that drive the model towards image borders during evolution. To implement the parametric model, we used a dynamic force formulation for the model [20] and we expressed it as a function of arc length and time. The following partial differential equation (PDE) was used for evolving the model:

$$\frac{\partial v}{\partial t} = \alpha \frac{\partial^2 v}{\partial s^2} - \beta \frac{\partial^4 v}{\partial s^4} + \kappa f_e + \lambda f_b \quad (2)$$

where $s$ is the arc length from an arbitrary point to all the other points on the curve; $t$ is the time, $\alpha$ and $\beta$ are constants that regulate the elasticity and rigidity of the model respectively; $f_e$ is the external force calculated from image data; $f_b$ is the balloon force that augments the external force in driving the model towards image borders; $\kappa$ and $\lambda$ are weighting parameters that determine the contribution of the external force and the balloon force respectively. The external force is computed as the negative gradient of the Gaussian filtered image. In order to start the evolution of the deformable model, empirically-determined weighting parameters for the model and the image forces as well as the initial position of the model are specified when calling the evolution function. The model was initialized as a circle centred at the approximated middle point of the bone of interest, with a radius equal to the width of the bone at this pixel level as shown in Fig. 3.

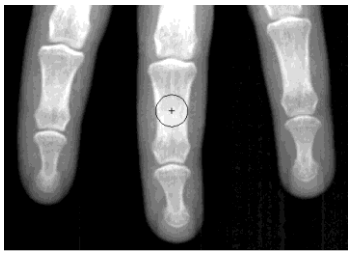

**Figure 3. Initialization of the deformable model (cross represents estimated centre of bone)**

### *D. Active Shape Model-based Segmentation*

ASMs use statistical models derived from example shapes for a particular object of interest. The ASM is trained by manually selecting landmarks describing the target shape in training images. A mean shape is computed through alignment, scaling, rotation and translation of the example shapes. The mean shape is then applied in test images and manipulated to find edges of an object with similar shape.

#### *1) Training*

We used excised bones for ASM training in order to avoid needless radiation exposure to participants. The museum in the Department of Human Biology at University of Cape Town provided 96 excised bones. The bones were divided into a training set of 30 bones for computing the mean ASM shape and a test set of 66 bones. Images of the bones were acquired as described at the beginning of Section II. Landmarks for the ASM were placed at the prominent features of the bone and two additional points were added between each pair of prominent features so that 46 points were used to fully describe the bone shape as shown in Fig 4.

The following algorithm was used to build the statistical shape model:

1. Obtain landmark coordinates for each shape in the training set using manual annotation.

2. Compute the mean normalized derivative profile for each landmark point and compute the covariance matrix of the mean normalized derivative profiles for each landmark.
3. Align the shapes of the training set.
4. Apply principal component analysis to find the weighting matrix to give more significance to those points with higher stability – these points have the least variation with respect to other points on the shape.
5. Calculate the statistical description of the training set shape coordinates:

$$x = x_m + P.b \quad (3)$$

where $x_m$ is the mean shape, $P$ is the matrix of the most significant eigenvectors of the covariance matrix and $b$ is vector of weights.

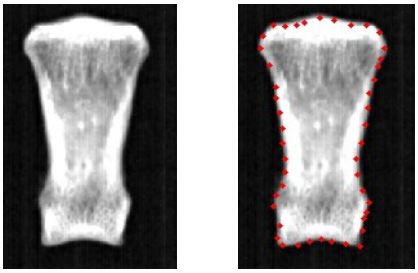

**Figure 4. ASM landmarks**

*2) Image search*

The first step in the search for the ROI is to initialize the ASM in the image. The final segmentation is highly dependent on the quality of the initialization and a good initialization is obtained by aligning the centroid of the mean shape with the centroid of the ROI. This was achieved by using the approximate centroid of the bone as discussed in Section B. The mean shape is scaled, rotated and translated so that the two centroids are aligned. The initial shape is shown to the user superimposed on the test image and the user is prompted to indicate whether the initial shape is good, too big or too small. The initial shape is automatically re-scaled if necessary and the user indicates if a better initialization is produced. Once the user indicates that the initialization is good, the search may begin. Fig. 5 shows an example of a good ASM initialization. A multi-resolution search is carried out using the image pyramid technique. The search ensures that the final shape resembles the mean shape and the Mahalanobis distance is employed to measure the similarity between the test shape and the mean shape.

**Figure 5. ASM initialization (cross represents estimated centre of bone)**

*E. Validation*

The segmentation accuracy of the two methods was determined by generating a ground truth through manual segmentation and comparing the bone contours extracted by the methods on a set of test images. Two graduate students were asked to perform manual segmentation of the test images under the guidance of a qualified radiographer and the average of the two contours was considered the ground truth. The Hausdorff distance measure [21] was used to quantify the similarity between the ground truth and the algorithm-determined contour in each image. The Hausdorff distance (HD) provides a measure of similarity between two sets of points and is defined as:

$$HD(A,B) = \max(h(A,B), h(B,A)) \quad (4)$$

where $A$ and $B$ are finite point sets and $h(A,B)$ is the directed Hausdorff distance from $A$ to $B$.

## III. RESULTS

The segmentation algorithms were applied to test images and the output of each method is a series of pixel points on the border of the bone of interest.

The ASM algorithm was first tested on 66 excised bone images and a comparison with manual segmentation showed close similarity and hence accurate segmentation, with an average Hausdorff distance of 5.72, a minimum of 3.74 and a and maximum of 8.58 pixels. To test the algorithms on the intended data type, 15 participants were recruited and images of their left hands were taken since BMD measurements are normally taken in the non-dominant hand. Table I summarizes the differences between contours detected by the two algorithms and manual segmentation while Fig 6 and Fig 7 show typical examples of the contours.

TABLE I. HAUSDORFF DISTANCE FOR HUMAN SUBJECTS

| Method | Hausdorff distance (pixels) | | |
|---|---|---|---|
| | *Mean* | *Minimum* | *Maximum* |
| ASM | 5.6(0.96) | 4.1 | 7.9 |
| Deformable model | 10.3(2.25) | 6.6 | 14.7 |

Standard deviation in brackets

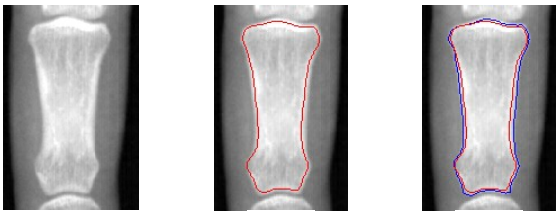

(a) (b) (c)

**Figure 6. An example of deformable model-based segmentation: a) test image b) detected contour c) detected contour (red) and manually drawn contour (blue) – Hausdorff distance, 6.57pixels**

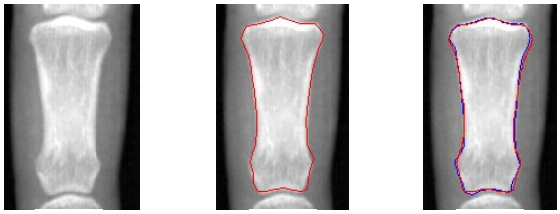

(a) (b) (c)

**Figure 7. An example of ASM-based segmentation: a) test image b) detected contour c) detected contour (red) and manually drawn contour (blue) – Hausdorff distance, 4.53pixels**

## IV. Discussion and Conclusion

The deformable model tends to converge far from the actual bone border. This can be solved by increasing the width of the Gaussian filter used in the calculation of the external image force or initialising the model outside the ROI. However the presence of other bones in close proximity to the bone of interest renders these possible solutions impractical as this would cause the model to be attracted to other bones. Even though only a small area of the bone is excluded by the deformable model, a great portion of this area is cortical bone and this is expected to distort BMD measurements. In contrast, the ASM tends to delineate the border of the bone with higher accuracy although it is also prone errors due to the presence of the other bones. However the initialization method used in this study reduces the chances of such errors occurring and the algorithm facilitates the correction of the initialization. An advantage of the deformable model algorithm is that it is completely automated and requires no user interaction. However, while user interaction is mandatory for the ASM algorithm, only one click of the mouse (indicating that the initialisation is good) is necessary in most cases due to the degree of automation for initialization; out of the 15 test images, only two images required correction for the initialization and no correction was required for the bone test images. The average Hausdorff distances obtained on the excised bones (5.7 pixels) and on human subjects (5.6 pixels) are almost equal and therefore the bone-trained ASM is suitable for segmenting actual hand images.

Gulam et al. [9] employed a deformable model for segmenting the middle phalanx of the middle finger and while they expressed satisfaction with the results, they did not validate the accuracy of the segmentations. Also, their deformable model was initialized by manually selecting points on the border of the bone. Unlike our automated technique, their method of initialization is time-consuming. Sotoca et al. [18] have used an ASM to segment the middle phalanx from hand radiographic images. However, they do not validate the accuracy of the segmentation but claim success based on results of BMD measurements based on the ASM segmentation. Their algorithm also relied on the user defined input for initialisation of the ASM. The result of ASM segmentation is highly dependent on initialization and having a user-defined starting point introduces subjectivity in the results. This is a drawback that has been addressed in this study.

In conclusion, the ASM technique is more accurate than a deformable model for segmenting the middle phalanx of the middle finger in digital radiographic images. The output of the segmentation algorithm can be used in estimating the BMD which in turn can be used to determine fracture risk and diagnosis of osteoporosis.

## References


[1] WHO. (2003). Prevention and management of osteoporosis. *World Health Organization Technical Report Series*, 921, 1-164.

[2] Blake, G. M., & Fogelman, I. (2010). An update on dual-energy X-ray absorptiometry. *Seminars in Nuclear Medicine*, 40(1), 62-73

[3] El Maghraoui, A., & Roux, C. (2008). DXA scanning in clinical practice. *QJM*, 101(8), 605-617.

[4] Vaananen, S. P., Isaksson, H., Julkunen, P., Sirola, J., Kroger, H., & Jurvelin, J. S. (2011). Assessment of the 3-D shape and mechanics of the proximal femur using a shape template and a bone mineral density image. *Biomech.Model.Mechanobiol*., 10(4), 529-538.

[5] Ralston, S. H. (2005). Bone densitometry and bone biopsy. *Best Pract.Res.Clin.Rheumatol*., 19(3), 487-501.

[6] Ross, P. (1997). Radiographic absorptiometry for measuring bone mass. *Osteoporosis Int.*, 7 (3), 103-107.

[7] Wasnich, R. D. (1998). Perspective on fracture risk and phalangeal bone mineral density. *J.Clin.Densitom*., 1(3), 259-268.

[8] Deodhar, A. A., Brabyn, J., Jones, P. W., Davis, M. J., & Woolf, A. D. (1994). Measurement of hand bone mineral content by dual energy x-ray absorptiometry: Development of the method, and its application in normal volunteers and in patients with rheumatoid arthritis. *Ann.Rheum.Dis.,* 53(10), 685-690.

[9] Gulam, M., Thornton, M. M., Hodsman, A. B., & Holdsworth, D. W. (2000). Bone mineral measurement of phalanges: Comparison of radiographic absorptiometry and area dual X-ray absorptiometry. *Radiology*, 216(2), 586-591.

[10] Hill, C. L., Schultz, C. G., Wu, R., Chatterton, B. E., & Cleland, L. G. (2010). Measurement of hand bone mineral density in early rheumatoid arthritis using dual energy X-ray absorptiometry. *Int.J.Rheum.Dis.,* 13(3), 230-234.

[11] Kwon, J. W., Cho, S. I., Ahn, Y. B., & Ro, Y. M. (2009). Noise reduction in DEXA image based on system noise modeling. *Biomedical and Pharmaceutical Engineering, 2009. ICBPE '09. International Conference on*, pp. 1-6.

[12] Pietka, E. (1995). Computer-assisted bone age assessment based on features automatically extracted from a hand radiograph. *Comput.Med.Imaging Graphics*, 19(3), 251-259.

[13] Levitt, T. S., Hedgcock, M. W.,Jr, Dye, J. W., Johnston, S. E., Shadle, V. M., & Vosky, D. (1993). Bayesian inference for model-based segmentation of computed radiographs of the hand. *Artif.Intell.Med*., 5(4), 365-387.

[14] Rucci, M., Coppini, G., Nicoletti, I., Cheli, D., & Valli, G. (1995). Automatic analysis of hand radiographs for the assessment of skeletal age: A subsymbolic approach. *Comput.Biomed.Res.*., 28(3), 239-256.

[15] Cheng, S. N., Chan, H. P., Niklason, L. T., & Adler, R. S. (1994). Automated segmentation of regions of interest on hand radiographs. *Med.Phys*., 21(8), 1293-1300.

[16] Cootes, T. F., Taylor, C. J., Cooper, D. H., & Graham, J. (1995). Active shape models-their training and application. *Comput.Vision Image Understanding*, 61(1), 38-59.

[17] Kass, ,Michael, Witkin, ,Andrew, & Terzopoulos, ,Demetri. (1988). Snakes: Active contour models. *International Journal of Computer Vision*, (4), 321-331.

[18] Sotoca, J. M., Iñesta, J. M., & Belmonte, M. A. (2003). Hand bone segmentation in radioabsorptiometry images for computerised bone mass assessment. *Comput.Med.Imaging Graphics*, 27(6), 459-467

[19] Otsu, N. (1979). A threshold selection method from gray-level histograms, *IEEE Trans. Sys., Man., Cyber,* 9, 62–66

[20] Chenyang Xu, & Prince, J. L. (1998). Snakes, shapes, and gradient vector flow. *Image Processing, IEEE Transactions on*, 7(3), 359-369.

[21] Huttenlocher, D. P., Klanderman, G. A., & Rucklidge, W. J. (1993). Comparing images using the hausdorff distance. *Pattern Analysis and Machine Intelligence, IEEE Transactions on*, 15(9), 850-863.